

An Assessment of the Southern Ocean Mixed Layer Heat Budget

SHENFU DONG,* SARAH T. GILLE, AND JANET SPRINTALL

Scripps Institution of Oceanography, University of California, San Diego, La Jolla, California

(Manuscript received 16 August 2006, in final form 24 January 2007)

ABSTRACT

The mixed layer heat balance in the Southern Ocean is examined by combining remotely sensed measurements and in situ observations from 1 June 2002 to 31 May 2006, coinciding with the period during which Advanced Microwave Scanning Radiometer-Earth Observing System (EOS) (AMSR-E) sea surface temperature measurements are available. Temperature/salinity profiles from Argo floats are used to derive the mixed layer depth. All terms in the heat budget are estimated directly from available data. The domain-averaged terms of oceanic heat advection, entrainment, diffusion, and air–sea flux are largely consistent with the evolution of the mixed layer temperature. The mixed layer temperature undergoes a strong seasonal cycle, which is largely attributed to the air–sea heat fluxes. Entrainment plays a secondary role. Oceanic advection also experiences a seasonal cycle, although it is relatively weak. Most of the seasonal variations in the advection term come from the Ekman advection, in contrast with western boundary current regions where geostrophic advection controls the total advection. Substantial imbalances exist in the regional heat budgets, especially near the northern boundary of the Antarctic Circumpolar Current. The biggest contributor to the surface heat budget error is thought to be the air–sea heat fluxes, because only limited Southern Hemisphere data are available for the reanalysis products, and hence these fluxes have large uncertainties. In particular, the lack of in situ measurements during winter is of fundamental concern. Sensitivity tests suggest that a proper representation of the mixed layer depth is important to close the budget. Salinity influences the stratification in the Southern Ocean; temperature alone provides an imperfect estimate of mixed layer depth and, because of this, also an imperfect estimate of the temperature of water entrained into the mixed layer from below.

1. Introduction

Southern Ocean mixed layer processes are an important component of the global climate system. One conceptual model of global meridional overturning circulation posits that water flows southward at middepth into the Southern Ocean where it is upwelled to the surface and carried northward through Ekman processes (e.g., Speer et al. 2000; Karsten and Marshall 2002; Marshall and Radko 2003). While at the ocean surface, water mass properties are transformed as water in the mixed layer interacts with the atmosphere. This

conceptual framework supposes that upper-ocean mixing effectively provides all of the diabatic mixing required to maintain the global overturning circulation.¹ Despite the hypothesized central role that Southern Ocean surface processes play in global circulation, the exact size and spatial structure of air–sea fluxes are not well known. In the Southern Ocean, available surface flux estimates from the National Centers for Environmental Prediction–National Center for Atmospheric Research reanalysis (NCEP–NCAR) and 40-yr European Centre for Medium-Range Weather Forecasts (ECMWF) Re-Analysis (ERA-40) can differ by

* Current affiliation: CIMAS/RSMAS, University of Miami, Miami, Florida.

Corresponding author address: Shenfu Dong, Scripps Institution of Oceanography, UCSD, 9500 Gilman Dr., Mail Code 0230, La Jolla, CA 92093-0230.
E-mail: shenfu.dong@noaa.gov

¹ The notion that interior diabatic mixing is negligible in the Southern Ocean may not hold up to detailed analysis of observations, which have suggested that subsurface diabatic mixing can be large in some locations, particularly near major topographic features (e.g., Naveira Garabato et al. 2004; Sloyan 2005; Thompson et al. 2007). This potentially results in nonnegligible subsurface diapycnal mixing on average but does not diminish the importance of surface mixing.

100 W m⁻² or more on any given day, compared with typical values of 150–250 W m⁻². The objective of this study is to provide a first step toward evaluating the consistency of the available data and to examine the specific mechanisms governing air–sea heat exchange within the mixed layer of the Southern Ocean.

Upper-ocean heat balances have been studied in some detail for western boundary current regions such as the Kuroshio Extension (Vivier et al. 2002), the Gulf Stream (Dong and Kelly 2004), and the East Australian Current (Roemmich et al. 2005), but the Southern Ocean has received comparatively little attention. Unlike western boundary current regions, where heat is transported from low to high latitudes, the Southern Ocean is dominated by the Antarctic Circumpolar Current (ACC), which primarily carries water zonally. Thus, while heat budgets in western boundary current regions are dominated by meridional geostrophic transport, geostrophic flow is expected to play a comparatively small role in the Southern Ocean. At the same time, the Southern Ocean experiences the largest surface westerly winds of the World Ocean, which are expected to drive large meridional Ekman transports.

Southern Ocean air–sea exchanges are important for a broad range of reasons beyond their importance to the meridional overturning circulation. The Southern Ocean has been implicated as one of the major regions of oceanic uptake of CO₂ (Caldeira and Duffy 2000; Sabine et al. 2004). The strong winds imply a potential for strong coupling between near-surface wind fields and underlying sea surface temperatures (SSTs). For example, O’Neill et al. (2003, 2005) found that the wind stress curl and divergence are linearly related to the cross- and downwind components of the SST gradient in the Agulhas Retroflexion region. Because the Southern Ocean is largely wind forced, changes in the wind field caused by SST gradients may in turn feed back into the ocean. Changes in SST along the ACC can redistribute heat in the Southern Ocean. Sun and Watts (2002) and Dong et al. (2006a), among others, have found that the ACC is warmer in the South Atlantic and Indian Oceans (where it is farther north) and is colder in the South Pacific (where it is closest to Antarctica).

Although direct observations in the Southern Ocean have historically been sparse, recent satellite measurements and new in situ observations provide some of the necessary data for a first examination of the upper-ocean heat balance. The Advanced Microwave Scanning Radiometer-Earth Observing System (EOS) (AMSR-E), launched in May 2002, for the first time provides SST data for the entire Southern Ocean with twice-daily temporal resolution. With its cloud-

penetrating ability, AMSR-E provides a unique dataset for examining the Southern Ocean heat balance. The wind field from Quick Scatterometer (QuikSCAT) scatterometry and the sea surface height (SSH) from altimetry can be used to estimate ocean Ekman and geostrophic heat advection, respectively, and their role in the heat budget. However, the lack of data is not the only factor that has prevented a detailed study of the heat balance in the Southern Ocean; validation of the available data in the Southern Ocean is another major factor. In particular, the air–sea heat fluxes have large uncertainties in the Southern Ocean because of the limited available in situ data. Thus, one challenge is to determine whether the existing data provide adequate information to close the upper-ocean thermal balance.

In this study, we evaluate whether the heat budget of the mixed layer closes in the Southern Ocean, using currently available remotely sensed measurements and in situ observations. To the extent that the budget does not close, what improvements are needed in the ocean observing system? In light of the distinct characteristics of the Southern Ocean, we would like to explore the potential differences of its upper-ocean heat balance compared with that in the western boundary current regions. Issues such as the relative role of the air–sea heat fluxes and oceanic processes in the heat balance, and the relative importance of the geostrophic versus the Ekman advection in the Southern Ocean will be addressed.

We start in section 2 with a simplified description of the processes governing the SST variability, followed by a discussion of the satellite measurements and in situ observations used in this study. All datasets (Table 1) used in this study are publicly available. The analyzed results of the surface ocean heat balance are described in section 3. In section 4, we examine the sensitivity of the heat balance to the different available datasets and the sensitivity of the surface water mass transformation to air–sea heat flux products. Conclusions are given in section 5.

2. Processes governing the SST variability

Variations in SST are governed through the heat balance in the surface mixed layer of the ocean, which is influenced by surface air–sea heat fluxes, horizontal advective and diffusive processes in the mixed layer, and entrainment processes at the base of the mixed layer. A schematic diagram of these processes is shown in Fig. 1. The equation for the mixed layer temperature is

$$\frac{\partial T_m}{\partial t} = \frac{Q_{\text{net}} - q(-h_m)}{\rho_0 c_p h_m} - \mathbf{u}_m \cdot \nabla T_m + \kappa \nabla^2 T_m - \frac{w_e \Delta T}{h_m}, \quad (1)$$

TABLE 1. Datasets used in the base case for the mixed layer heat budget. Details of their sources are listed in the acknowledgments.

Variables		Source
Mixed layer temperature, T_m		AMSR-E SST (Dong et al. 2006b)
Air-sea heat fluxes, Q_{net}	Latent sensible	Derived from COARE 3.0 algorithm (Fairall et al. 2003) using NCEP-NCAR I variables
	Longwave, shortwave	NCEP-NCAR Reanalysis I (Kalnay et al. 1996)
SSH, η	Anomalies	AVISO (Ducet et al. 2000)
	Mean	Maximenko and Niiler (2005)
Wind stress, τ		COAPS pseudostress (Pegion et al. 2000) converted to stress using parameters from Yelland and Taylor (1996)
Mixed layer depth, $h_m(\rho)$		Argo float profiles (Gould et al. 2004), based on density criterion $\Delta\rho = 0.03 \text{ kg m}^{-3}$ (de Boyer Montegut et al. 2004)
ΔT		Argo float profiles, corresponding to $h_m(\rho)$
Eddy diffusivity, κ		$500 \text{ m}^2 \text{ s}^{-1}$

where T_m is the mixed layer temperature, h_m is the mixed layer depth, w_e is the entrainment velocity, ΔT is the temperature difference between the mixed layer and just below the mixed layer, κ is eddy diffusivity (set to be $500 \text{ m}^2 \text{ s}^{-1}$), ρ_0 (1027 kg m^{-3}) is the reference density of seawater, and c_p ($4000 \text{ J kg}^{-1} \text{ K}^{-1}$) is the specific heat of seawater at constant pressure. Here Q_{net} denotes the net surface heat flux, which is positive into the ocean, and $q(-h_m)$ is the downward radiative heat flux at the bottom of the mixed layer. The horizontal velocity \mathbf{u}_m includes both the geostrophic (\mathbf{u}_g) and Ekman (\mathbf{u}_e) components.

The Kraus–Turner-type mixed layer model of Eq. (1), together with an equation for mixed layer depth h_m (not shown), are often used to predict T_m and h_m (Qiu and Kelly 1993; Vivier et al. 2002; Dong and Kelly 2004). In this study, instead of solving for T_m and h_m , we attempt to close the heat balance using T_m and h_m

data from observations. Here the T_m field comes from SST observations of the AMSR-E satellite data. A detailed description of the AMSR-E SST can be found in Dong et al. (2006a,b). AMSR-E data are on a 0.25° longitude \times 0.25° latitude grid. Four years (1 June 2002–31 May 2006) of weekly SST observations from version-5 AMSR-E ocean products are used in this study to determine the T_m tendency [left-hand side of (1)]. The AMSR-E SST is masked over land and ice; hence, all terms in (1) are estimated only over open water.

The mixed layer depth h_m is computed from Argo float profiles of temperature, salinity, and pressure (Gould et al. 2004). Although Argo deployments began in 2000, only profiles collected during the AMSR-E time period and with a “good” quality flag are used. Most of the profiles are from north of 60°S . De Boyer Montegut et al. (2004) recently produced a monthly

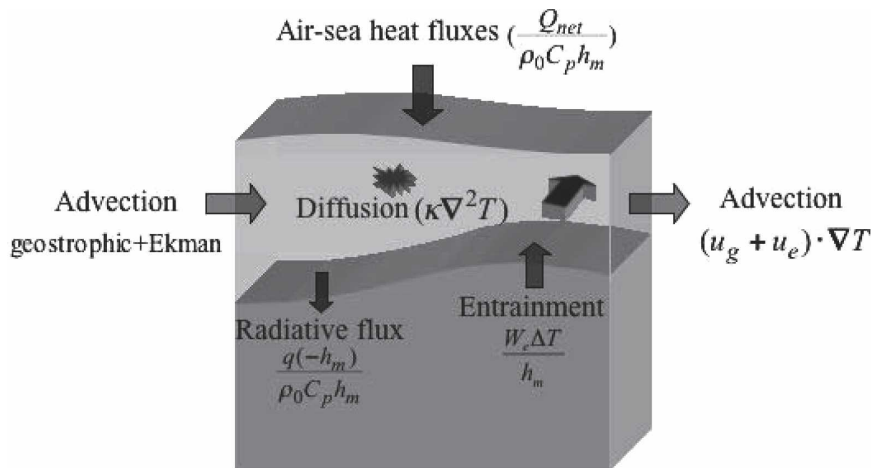


FIG. 1. Schematic diagram showing the processes governing the mixed layer temperature variations.

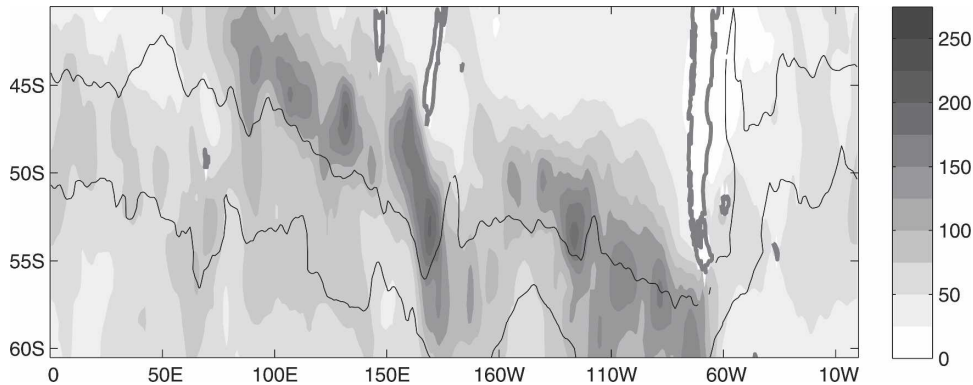


FIG. 2. Annual mean mixed layer depth (m) derived from Argo float profiles. The ACC is defined by a northern (-0.4 m) and southern (-1.2 m) SSH contour (black lines) from Maximenko and Niiler (2005).

climatological h_m using hydrographic profiles available from 1941 through 2002 from mechanical bathythermograph (MBT), expendable bathythermograph (XBT), conductivity–temperature–depth (CTD), and profiling float data. However, the coverage of these available data in the Southern Ocean is sparse, particularly for salinity. De Boyer Montegut et al. (2004) suggested that individual profiles yield h_m values that are about 25% deeper than those from climatological temperature/salinity profiles. We follow de Boyer Montegut et al. (2004) and determine h_m from individual float profiles based on a density criterion, $\Delta\rho = 0.03 \text{ kg m}^{-3}$, where $\Delta\rho$ is the density difference from the top-most near-surface value. A monthly climatology is then objectively mapped (Roemmich 1983) from those individual h_m using a decorrelation scale of 2° latitude \times 5° longitude and 30 days in time. This monthly climatology is generally deeper than that of de Boyer Montegut et al. (2004). The monthly climatology is linearly interpolated to weekly values for use in (1). Figure 2 shows the annual mean h_m . Deep mixed layers are generally found just north of the ACC, here defined as a circumpolar band between the mean dynamic heights of -0.4 and -1.2 m.

The net surface heat flux Q_{net} is defined so that positive fluxes are directed into the ocean. As mentioned before, the uncertainties of surface heat flux products in the Southern Ocean are large compared to other oceanic regions because in situ observations are sparse. (Formal statistical uncertainties are unknown, because none of the reanalysis flux products are released with statistical error estimates.) The surface heat fluxes from NCEP–NCAR are the only flux product publicly available during our entire study period. However, Renfrew et al. (2002) found that the NCEP–NCAR products systematically overestimate the sensible and latent heat

fluxes in moderate to high wind conditions. They recommended recalculating the surface heat fluxes using a more appropriate bulk algorithm. Here we calculate the latent and sensible heat fluxes from the state-of-the-art bulk flux algorithm version 3.0 developed from the Coupled Ocean–Atmosphere Response Experiment (COARE3.0; Fairall et al. 2003). The input variables (SST, air temperature, surface wind speed, surface pressure, and air specific humidity) and the net longwave and shortwave radiative fluxes are from the NCEP–NCAR daily product, which is on a Gaussian grid with 2° resolution in both zonal and meridional directions. The COARE3.0 algorithm gives relatively weak latent and sensible heat fluxes compared to the NCEP–NCAR product (Fig. 3), though the spatial distributions are similar (Figs. 3b–e). Both latent and sensible heat fluxes show a weak seasonal cycle with strong fluxes during winter (Fig. 3a). The latent heat fluxes are 5 times larger than the sensible heat fluxes. The daily fluxes are averaged to match the weekly AMSR-E SST resolution. The weekly fluxes are then interpolated to a $1^\circ \times 1^\circ$ grid. An autocorrelation analysis indicates that the fluxes derived from NCEP–NCAR variables have an e -folding scale of 6° latitude and 12° longitude, suggesting that the heat fluxes are potentially smoother than the AMSR-E SST fields.

The downward radiative heat flux at the bottom of the mixed layer $q(-h_m)$ is derived from the NCEP–NCAR solar radiation values based on an assumption of exponential decay with depth (Paulson and Simpson 1977; Qiu and Kelly 1993),

$$q(-h_m) = q(0)[Re^{(-h_m/\gamma_1)} + (1 - R)e^{(-h_m/\gamma_2)}], \quad (2)$$

where $q(0)$ is the downward shortwave radiative flux at the sea surface; and R , γ_1 , and γ_2 are constants depend-

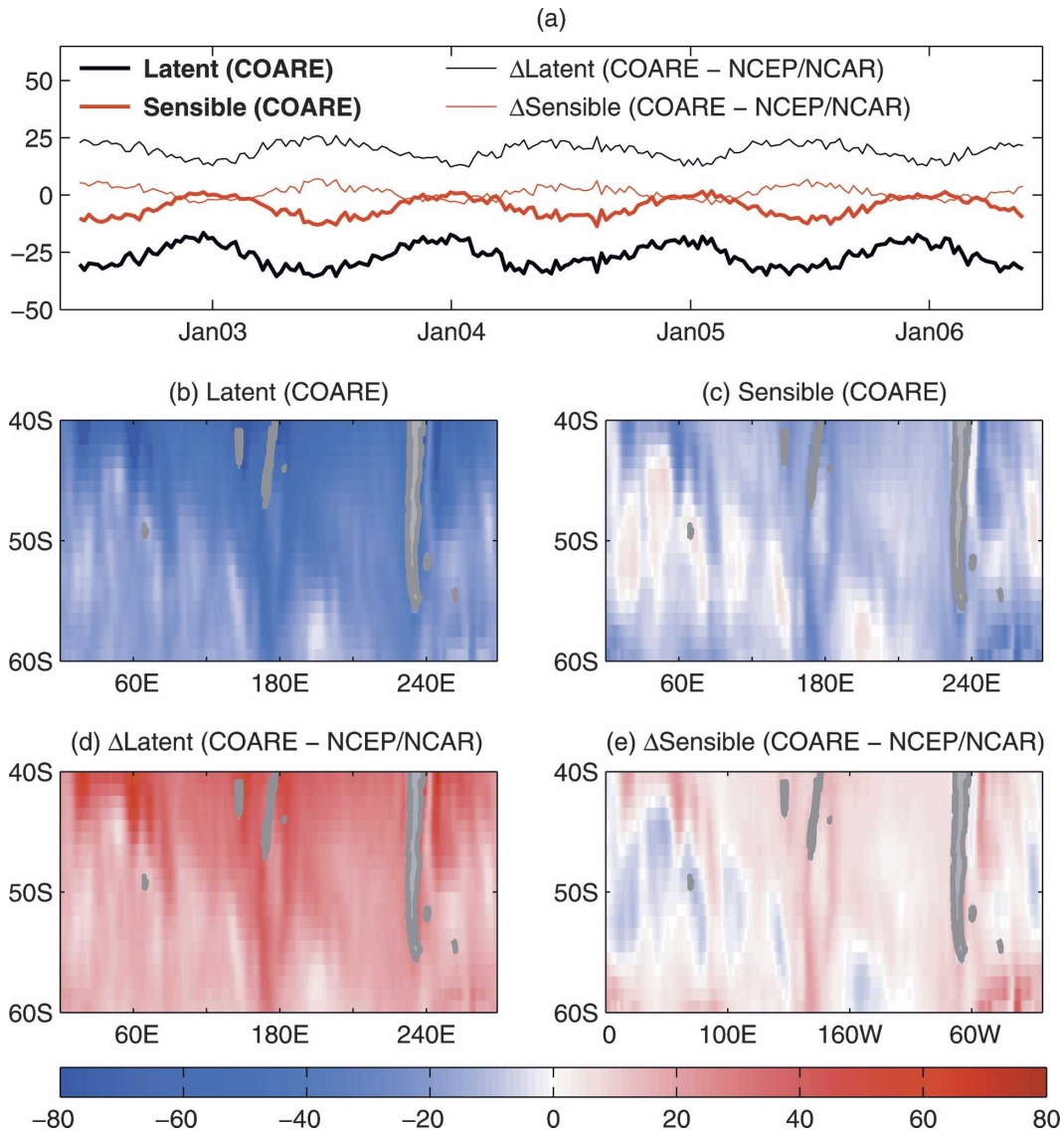


FIG. 3. (a) Domain-averaged latent (thick black line) and sensible (thick red line) heat fluxes from COARE3.0, and their differences from the NCEP-NCAR product (latent: thin black line, sensible: thin red line). June averages of (b) latent and (c) sensible heat fluxes from COARE3.0, and differences of (d) latent and (e) sensible heat fluxes between COARE3.0 and NCEP-NCAR reanalysis. Units: W m^{-2} .

ing on the water properties. Jerlov (1968) defines five types of ocean water (I, IA, IB, II, and III), ranging from clear to turbid. Water types IB and II correspond to chlorophyll concentration close to 0.1 and 0.5 mg m^{-3} , respectively. The mean chlorophyll concentration in the Southern Ocean is less than 0.3 mg m^{-3} (Moore and Abbott 2000). Thus, values for R (0.67), γ_1 (1.0), and γ_2 (17.0) corresponding to water type IB are used in this study. Using values for water type II does not change our results significantly. In general, $q(-h_m)$ is less than 20 W m^{-2} , which is relatively small compared to the uncertainty of Q_{net} in the Southern Ocean.

The oceanic advection term ($\mathbf{u}_m \cdot \nabla T_m$) includes both the geostrophic ($\mathbf{u}_g \cdot \nabla T_m$) and Ekman ($\mathbf{u}_e \cdot \nabla T_m$) components. The geostrophic component (\mathbf{u}_g) is evaluated using the total SSH field (η) $\mathbf{u}_g = -g\nabla\eta \times \hat{\mathbf{k}}/f$, where f is the Coriolis parameter, and $\hat{\mathbf{k}}$ is the vertical unit vector. We make use of the merged SSH altimeter products produced by Archiving, Validation and Interpretation of Satellite Oceanographic (AVISO) data using all the available satellites [Ocean Topography Experiment (TOPEX)/Poseidon, *Jason-1*, the first and second European Remote Sensing Satellites (*ERS-1* and *-2*, respectively), Environmental Satellite (Envi-

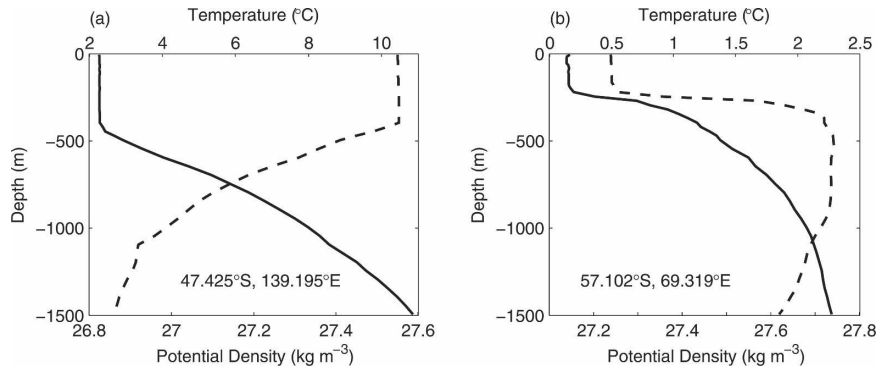


FIG. 4. Temperature (dashed line) and density (solid line) profiles from Argo floats for (a) a typical stratification profile of increasing density and decreasing temperature with depth, and (b) a profile with a temperature inversion.

sat), GeoSat Follow-On Satellite (GFO)] on a 3.5-day temporal resolution and a $1/3^\circ \times 1/3^\circ$ spatial resolution (Ducet et al. 2000). To determine the total SSH, we add to the anomalous SSH altimeter maps a mean dynamic ocean topography from Maximenko and Niiler (2005). This mean dynamic topography combines measurements from the Gravity Recovery and Climate Experiment (GRACE) with hydrography and surface drifter observations. We will later examine implications of using an alternative mean SSH field for the heat budget.

We use pseudostress fields from the Center for Ocean–Atmospheric Prediction Studies (COAPS) to estimate the Ekman velocity \mathbf{u}_e , which is related to the surface wind stress ($\boldsymbol{\tau}$) by $\mathbf{u}_e = \boldsymbol{\tau} \times \hat{\mathbf{k}} / \rho_0 f h_m$. The COAPS gridded wind fields are objectively mapped onto a $1^\circ \times 1^\circ$ grid from QuikSCAT measurements (Pegion et al. 2000). We compute 6-hourly stress fields using parameters from Yelland and Taylor (1996) and average to produce weekly wind stress. Here we use h_m as the Ekman depth because we lack knowledge of the true Ekman depth in the Southern Ocean. The sensitivity of the heat budget to this approximation will be examined in section 4.

The last term on the right-hand side of (1) describes the entrainment of water from below the base of the mixed layer. The entrainment velocity (w_e) is determined from the turbulent kinetic energy balance, which is controlled by wind stirring and a stabilizing effect resulting from surface heating. A detailed description of w_e can be found in Dong and Kelly (2004). The NCEP–NCAR fluxes and wind stress from COAPS are used to calculate w_e . The entrainment velocity is set to be zero during the detraining period.

In many heat budget studies the temperature difference (ΔT) between the mixed layer and just below the mixed layer is set to a constant (Qiu and Kelly 1993; Qiu 2000; Vivier et al. 2002; Dong and Kelly 2004). The

0.03 kg m^{-3} density criterion used to define h_m corresponds to $\Delta T = 0.2^\circ\text{C}$ if salinity effects are ignored. However, while the salinity effect may be negligible in other oceanic regions, it is not in the Southern Ocean, especially south of the polar front where salinity dominates the stratification (Pollard et al. 2002). Figure 4a shows an example of a typical stratification profile of increasing density and decreasing temperature with depth, and Fig. 4b shows a profile with a temperature inversion. In this study, we compute ΔT directly from the temperature profiles of the Argo floats. A monthly climatology of ΔT is objectively mapped from individual ΔT values, much like our h_m climatology. The temperature difference experiences a seasonal cycle with high ΔT during summer (Fig. 5a) and low ΔT during winter (Fig. 5b). Temperature inversions are typical south of the ACC and in the Indian Ocean (Fig. 5b, $40^\circ\text{--}50^\circ\text{S}$, $70^\circ\text{--}150^\circ\text{E}$) during winter (Fig. 5b). The presence of a temperature inversion implies that the mixed layer can actually warm by entraining warmer water from below, contradicting the traditional idea of cooling by entrainment. The presence of temperature inversions also suggests that salinity observations are important in the Southern Ocean.

3. Heat balance

The heat balance is examined over the entire Southern Ocean ($40^\circ\text{--}60^\circ\text{S}$, $0^\circ\text{--}360^\circ$). To estimate each term of the heat balance in (1), we interpolated all variables onto a $1^\circ \times 1^\circ$ grid with weekly temporal resolution for our 4-yr study period. The e -folding scales of variables other than heat fluxes are relatively small; for example, the e -folding scales of SST and SSH are less than 2° in both latitude and longitude. To match roughly the spatial resolution of the air–sea heat fluxes, we smoothed the SST and SSH maps and the wind fields using a $6^\circ \times 6^\circ$ triangle filter. This spatial filter and the weekly tem-

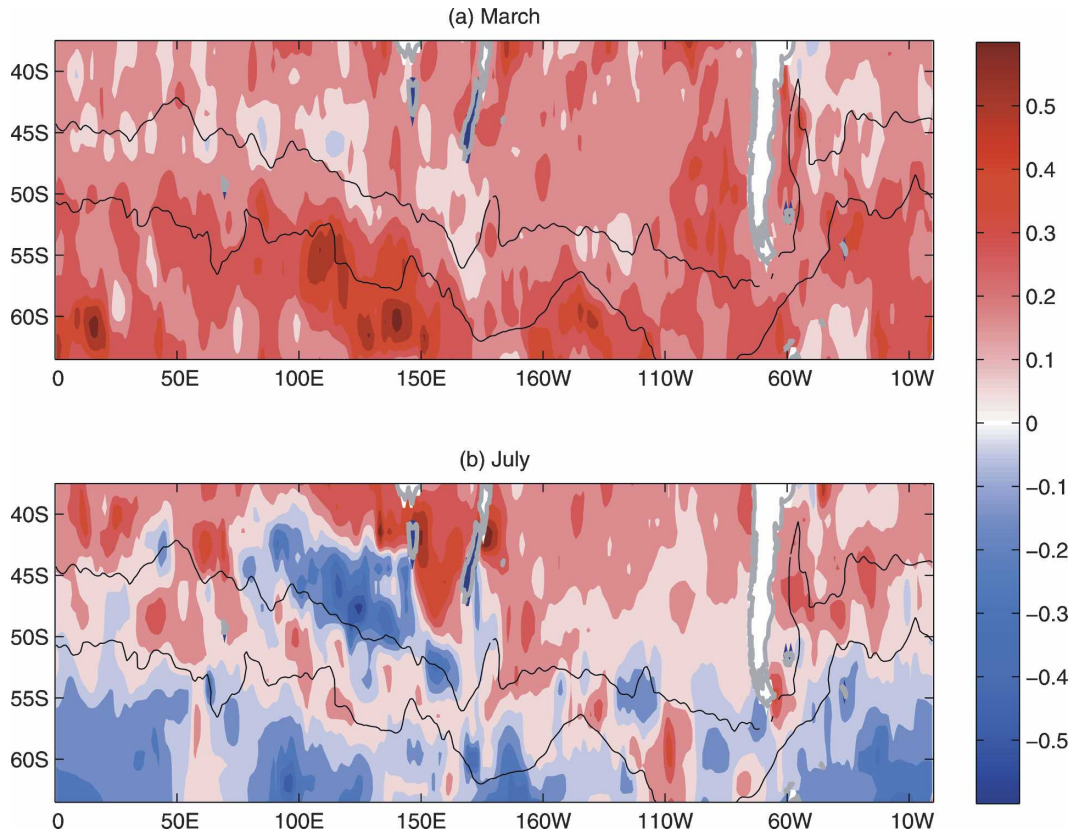


FIG. 5. Temperature difference ($^{\circ}\text{C}$) between the mixed layer and just below the mixed layer from Argo float profiles for (a) March and (b) July. As in Fig. 2, the black lines define the ACC.

poral resolution will suppress the effect of the meso-scale eddies and synoptic weather events for this analysis.

a. Domain average

Before we examine the spatial distribution of the heat balance, we first evaluate how well the heat balance closes on the scale of the entire Southern Ocean. The domain-averaged temperature tendency (Fig. 6a) compares well with the sum of contributions from the other terms. The error bars in Fig. 6 correspond to two standard errors for each term, where one standard error is equivalent to one standard deviation divided by the square root of the number of independent observations, which is defined as the number of observations divided by the decorrelation scales in both space and time. The temperature tendency is dominated by the seasonal cycle. The surface ocean is warmed during spring and summer and cooled during fall and winter. This seasonal cycle is mainly controlled by the surface heat fluxes, which is consistent with a regional study in the southeastern Indian Ocean (Sallee et al. 2006). The second largest term is the vertical entrainment, which is

always negative in the domain average. Entrainment experiences a seasonal cycle, reaching its maximum in March and decreasing to zero in most regions during October–December. The advection term is also always negative throughout the year. The maximum cooling effect due to advection occurs in January/February, and is slightly smaller than the maximum cooling due to the entrainment term. The diffusion term is very small and does not contribute to the T_m seasonal cycle in the domain average. As in the Gulf Stream region (Dong and Kelly 2004), there is a phase difference between the starting time of cooling in T_m and that of the negative surface heat flux. The T_m starts to cool at the end of February, but the heat loss to the atmosphere does not start until the end of March. Both advection and entrainment are responsible for this phase difference. Although heat is still fluxing into the ocean in February, part of that heat is mixed deeper into the water column via the entrainment term, and part of it is transported to the north via Ekman advection.

The sum of all the terms captures not only the seasonal cycle in the temperature tendency, but also the short-term fluctuations. These fluctuations are mostly

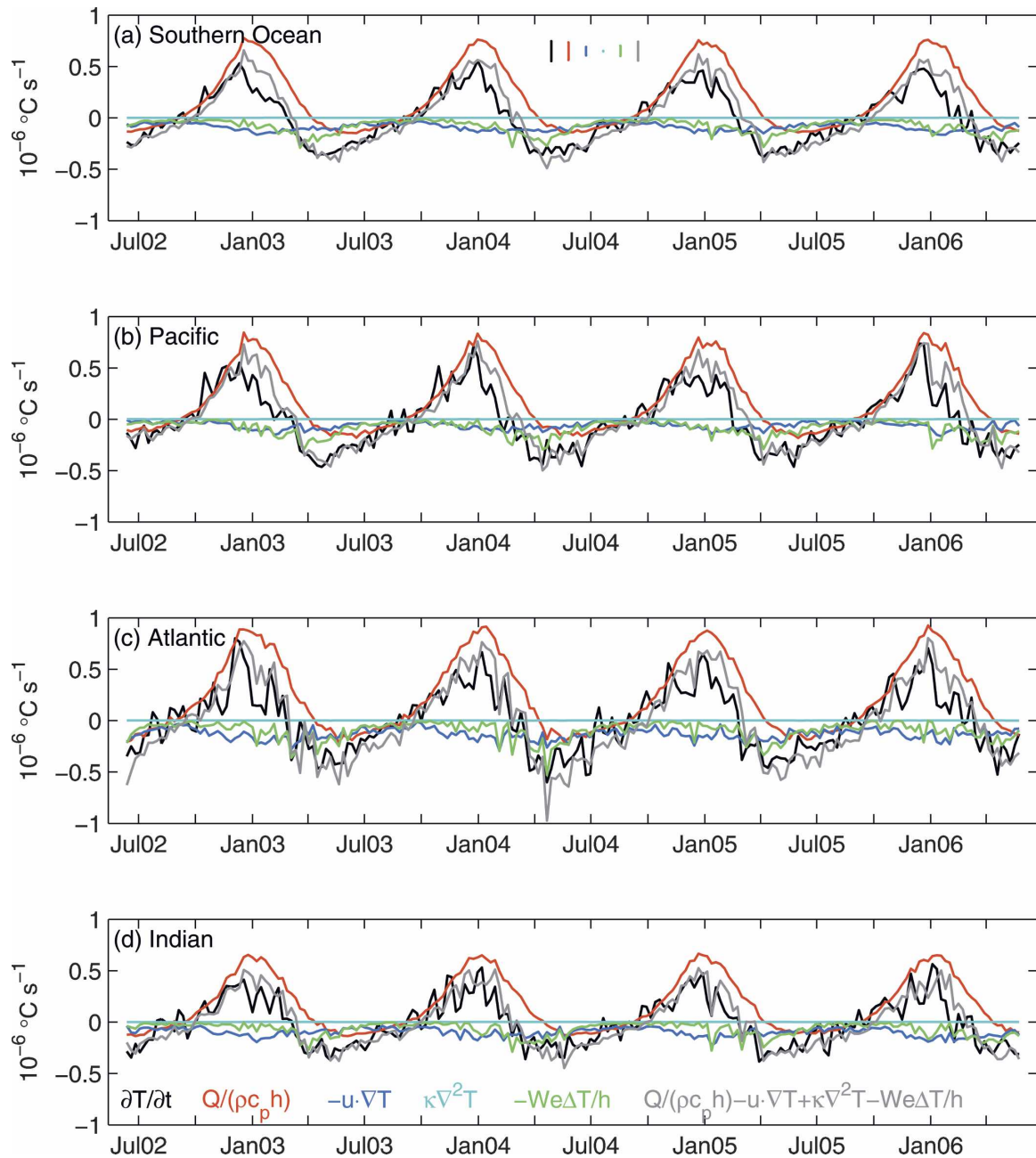


FIG. 6. (a) Domain-averaged heat budget in the Southern Ocean (40° – 60° S), and heat budget averaged in the (b) Pacific, (c) Atlantic, and (d) Indian sectors of the Southern Ocean. The gray curve is the sum of the contributions of surface heating (red), oceanic advection (blue), diffusion (cyan), and vertical entrainment (green) to the temperature tendency (black). The vertical lines in (a) correspond to two standard errors for each term. One standard error is equivalent to one standard deviation divided by the square root of the number of independent observations.

controlled by entrainment and advection (Fig. 6a), possibly due to from short-term fluctuations in the wind field.

We also examined the heat balance averaged in the three ocean basins (Figs. 6b,c,d), which shows results similar to the domain average with the seasonal cycle in

T_m controlled by surface heating. The T_m seasonal cycle is strongest in the Atlantic (Fig. 6c) and weakest in the Indian Ocean (Fig. 6d).

A number of studies have noted that upper-ocean processes differ on either side of the polar front within the ACC (e.g., Thompson et al. 2007). To examine geo-

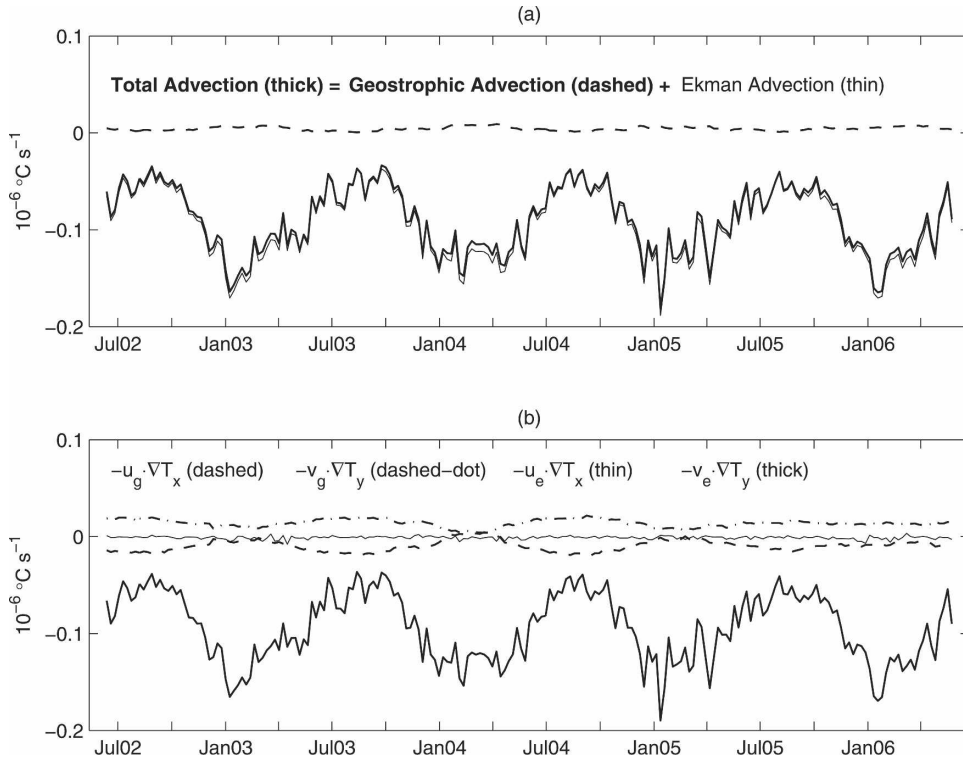


FIG. 7. (a) Contributions of the geostrophic (dashed line) and Ekman (thin line) components to the total advection (thick line) in $10^{-6} \text{ } ^\circ\text{C s}^{-1}$. (b) Zonal and meridional components in the advection.

graphic differences in the heat balance, we divided the region into the following three areas: north of, south of, and within the ACC. However, our results (not shown) do not indicate significant differences in these three areas.

Dividing advection into geostrophic and Ekman components (Fig. 7a), we find that the contribution of the geostrophic advection is negligible. Most of the variations in the advection term come from the Ekman advection. We further divide the advection into zonal and meridional components (Fig. 7b). Both zonal and meridional components of the geostrophic advection are relatively small compared to the meridional Ekman advection, and they also compensate each other. This is not surprising because geostrophic flow follows SSH contours, and SSH contours are nearly parallel to SST contours within the Southern Ocean. Figure 7b shows that the meridional component of the Ekman transport dominates; the strong westerlies in the Southern Ocean and the large meridional SST gradient contribute to the northward heat transport. Both the meridional Ekman velocity and the SST gradient show a seasonal cycle coherent with the Ekman advection. However, neither the Ekman velocity nor the SST gradient is the major factor for the seasonal cycle in the advection. We will show below that the seasonal cycle in the advection can

be largely attributed to seasonal variations in the mixed layer depth.

Although the surface heating term dominates the seasonal evolution of the mixed layer temperature, an accurate representation of the seasonal cycle in h_m is also important to the seasonal cycle in T_m . To illustrate the sensitivity of the heat budget to the seasonal cycle in h_m , we compute each term using the temporal mean (\bar{h}_m) of the monthly h_m climatology from Argo floats (Fig. 8a). As expected, because of the absence of the seasonal variation in \bar{h}_m , the amplitude of the seasonal cycle in each term decreases compared to Fig. 6a. In particular, the time-averaged \bar{h}_m results in less surface warming in summer, because \bar{h}_m exceeds summer h_m , and it results in increased surface cooling in winter when h_m exceeds \bar{h}_m . More interestingly, the seasonal variations in the Ekman advection disappear (Fig. 8b), indicating that the seasonal signal in advection can be attributed to the seasonal cycle in h_m . This is consistent with the fact that the wind stress experiences very weak seasonal variations in the Southern Ocean (Gille 2005). The magnitude of the advection increases slightly during winter and decreases substantially during summer. The role of the annual cycle of h_m in the heat balance suggests that the interannual variations in h_m may also play a role in the interannual variations in the mixed

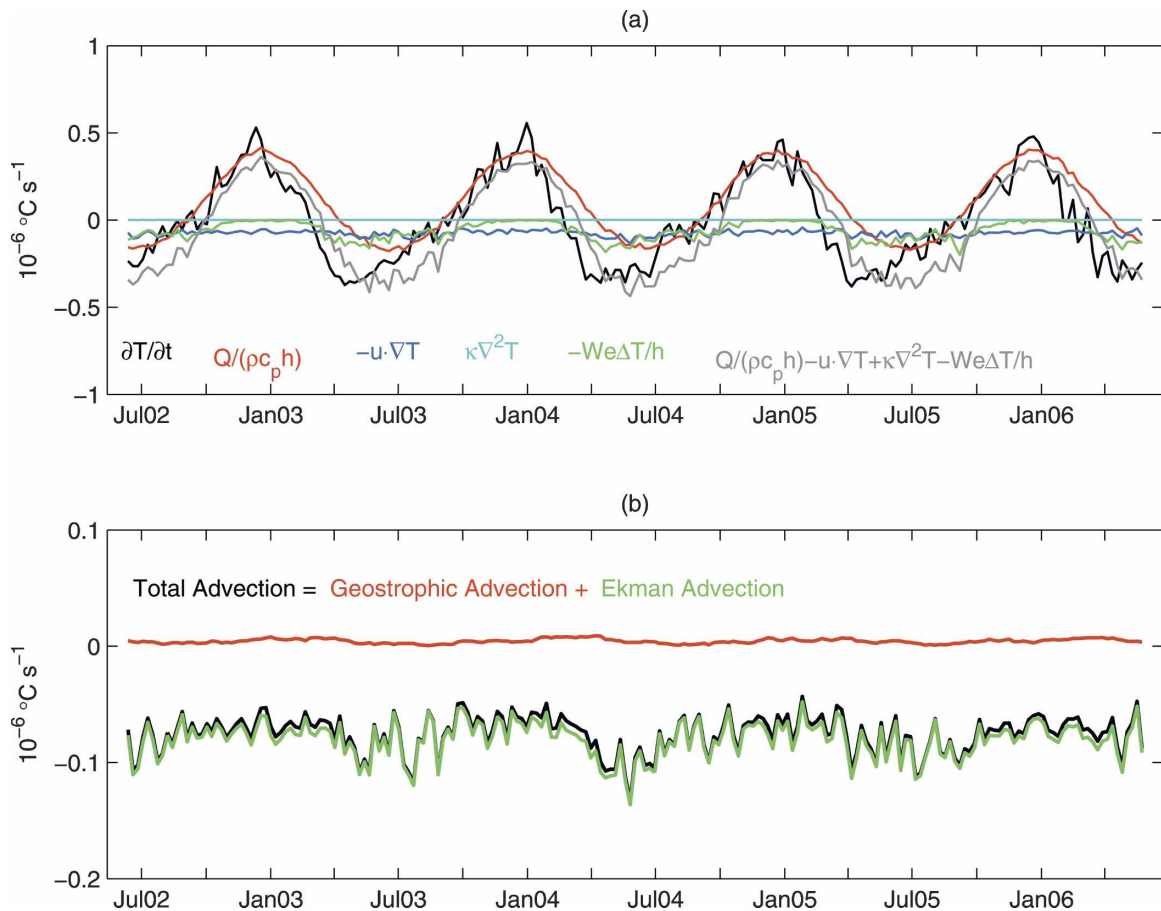


FIG. 8. (a) Domain-averaged terms of the heat budget with a time-mean mixed layer depth. The gray curve is the sum of the contributions from surface heating (red), oceanic advection (blue), diffusion (cyan), and vertical entrainment (green) to the temperature tendency (black). (b) Oceanic advection and its two components: geostrophic and Ekman. Units: $10^{-6} \text{ }^{\circ}\text{C s}^{-1}$.

layer heat balance. A number of coupled air–sea models have treated the ocean as a fixed-depth slab (e.g., Bladé 1997; Barsugli and Battisti 1998). The above result suggests that to get a better upper-ocean thermal balance involving the air–sea heat exchange, a proper representation of the temporal variations of h_m is required.

b. Spatial variation

The zonal average of each term as a function of latitude (not shown) resembles the domain average. With the exception of diffusion, all terms undergo a strong seasonal cycle. The surface heating term decreases toward high latitudes owing to the decreasing solar insolation.

To examine the spatial distribution of each term, we computed the monthly averages. Figure 9 shows all the individual components in (1) and their sum during March (Figs. 9a–f) and November (Figs. 9g–l). The

phase difference between temperature tendency and the negative surface heat fluxes in Fig. 6a during March is seen clearly in Figs. 9a,c; the temperature tendency is negative in general, whereas the surface heating term is mostly positive. In March, entrainment (Fig. 9f) and advection (Fig. 9d) both have a large effect in the Brazil–Falkland confluence region (60° – 30°W). In this region, entrainment and advection not only balance the warming from surface heat fluxes, but they also contribute to the cooling of the SST. The advection term is also large in the Agulhas Return Current region (40° – 50°S , 0° – 100°E). This suggests that oceanic processes may play an important role in those regions. The advection term (Fig. 9d) shows a small-scale structure along the ACC where the horizontal temperature gradient is strong. However, the surface heating term (Fig. 9c) does not resolve this small-scale structure, suggesting that even after filtering the other fields, the NCEP–NCAR products are probably still too smooth. Strong cooling from entrainment is also seen in the Indian

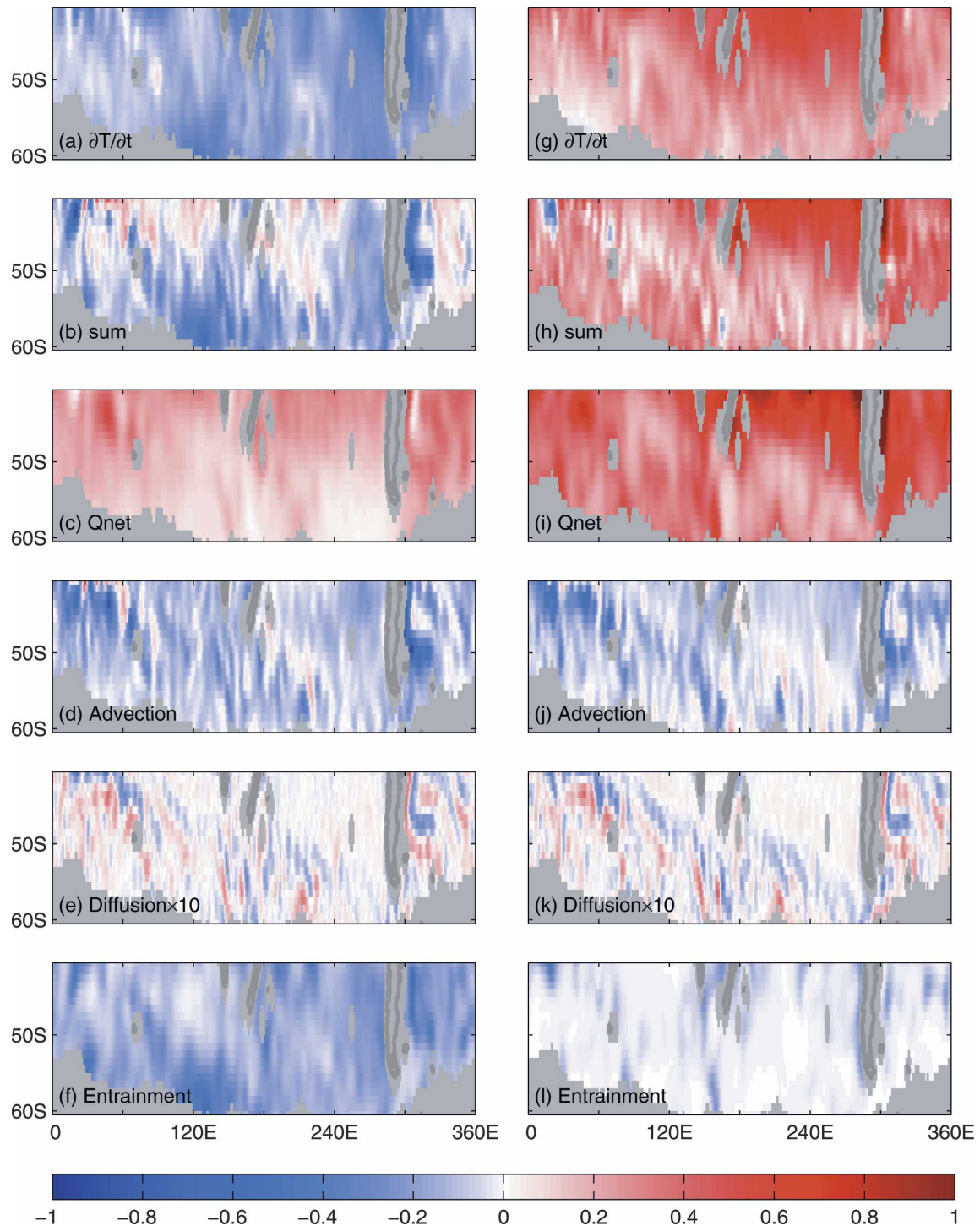


FIG. 9. (a)–(f) March and (g)–(l) November averages of the (a), (g) SST tendency, (b), (h) sum of all the contributions to the temperature tendency, (c), (i) surface heating, (d), (j) oceanic advection, (e), (k) diffusion ($\times 10$), and (f), (l) vertical entrainment. Units: $10^{-6} \text{ }^{\circ}\text{C s}^{-1}$.

Ocean (53° – 60°S , 100° – 150°E) and in the Pacific (40° – 45°S , 170° – 80°W). Warming from the surface heat fluxes during November (Fig. 9i) is reduced mainly by advection (Fig. 9j). Entrainment is weak during this

warming phase (Fig. 9l). Although its magnitude is small, the spatial distribution of advection during November (Fig. 9j) is similar to that during March (Fig. 9d). Again, the small-scale structure in advection (Fig.

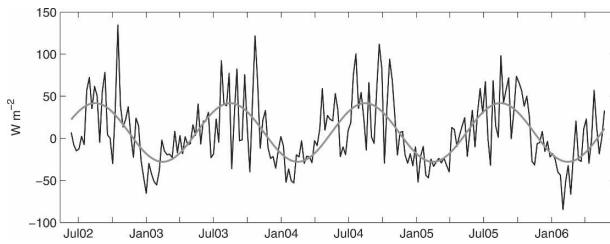


FIG. 10. Domain-averaged imbalance (black line) and the annual cycle of the imbalance (gray line).

9j) is not captured by surface heating (Fig. 9i). To close the mixed layer heat budget, we probably need a better heat flux product that resolves these small-scale features in the temperature field.

If all data were perfect, Figs. 9a,b would be expected to be the same, as would Figs. 9g,h. Although the temperature tendency can be explained by the sum of all the terms in the domain average (Fig. 6a), large differences at individual locations appear in Figs. 9a–f and in Figs. 9g–l, especially within the ACC. Details of the differences are discussed in the next section.

c. Imbalance

In this section we examine the imbalance (δ) in (1), defined as the difference between the temperature tendency and the sum of all other terms, that is, the difference between the thick and thin black lines in Fig. 6a. We first examine the domain-averaged imbalance. The imbalance (Fig. 10) varies seasonally with a minimum in January/February of about -27 W m^{-2} and a maximum in August/September of about 45 W m^{-2} . During winter the imbalance shows higher fluctuations compared to the relatively stable imbalance during summer.

Many factors can contribute to the imbalance, includ-

ing errors in the surface heat fluxes, velocity fields, entrainment, and estimates of the mixed layer depth. Of these factors, the surface heat fluxes are expected to be the largest contributor to the surface heat budget error, because only limited Southern Hemisphere data are available for the reanalysis products, and hence the reliability of these fluxes is uncertain. In particular, the lack of in situ measurements during winter is of fundamental concern, and this could explain the large imbalance during winter (Fig. 10). A detailed examination of the contributions to the imbalance from a number of factors, such as surface heat fluxes and mixed layer depth, is given in the next section.

To examine the spatial distribution of the imbalance, we computed the root-mean-square imbalance $\text{rms}(\delta)$ at each grid point, $\text{rms}(\delta) = \sqrt{\sum \delta_i^2/n}$, where δ_i is the imbalance at time i and n is the number of data points at a given geographic location. The imbalance (Fig. 11) is relatively large around the northern boundary of the ACC, where h_m is deepest (Fig. 2) and the horizontal temperature gradient is strong (not shown). Short time- and small-scale coupling is expected between surface wind and SST in the vicinity of the SST fronts (Chelton et al. 2004). Because the Southern Ocean is largely wind forced, the effect of SST on the wind field, as suggested by O'Neill et al. (2003, 2005), may feed back to the SST. The large imbalance near the ACC (Fig. 11) suggests that potential complex coupling and feedback processes in this region may not be well resolved by the existing measurements. Examination of $\text{rms}(\delta)$ for summer and winter separately (not shown) indicates that the large imbalance around the northern boundary of the ACC mostly occurs during winter. The low number of winter observations and the strong response of the wind field to the underlying SST during winter (O'Neill et al. 2005) probably both contribute to the large wintertime imbalance.

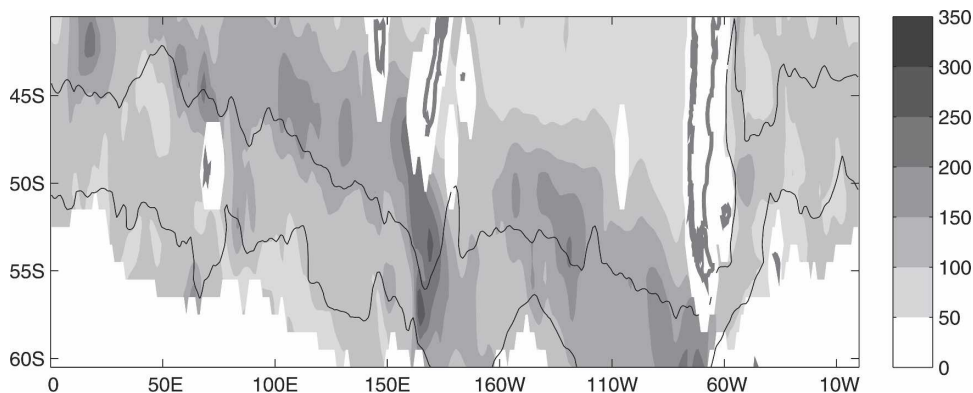


FIG. 11. Spatial distribution of the root-mean-square (rms) of the imbalance (W m^{-2}). As in Fig. 2, the black lines define the ACC.

TABLE 2. Comparison of the rms imbalance of the mixed layer heat budget. Variables and datasets used in the base case are listed in Table 1. In each row, except for the variable listed in the left-hand column, the other input data for the heat budget remain the same as the base case; T and ρ indicate that h_m is derived based on temperature criterion and density criterion, respectively. (Stars indicate the rms imbalance with the outliers removed.)

rms(δ) \pm 2 standard error	ΔT from Argo		$\Delta T = 0.2^\circ\text{C}$	
	$10^{-7} \text{ }^\circ\text{C s}^{-1}$	W m^{-2}	$10^{-7} \text{ }^\circ\text{C s}^{-1}$	W m^{-2}
Base case	3.26 ± 0.12	127.8 ± 4.9	3.69 ± 0.14	137.8 ± 5.2
h_m from Argo (T)	3.37 ± 0.13	129.3 ± 4.9	3.46 ± 0.13	135.5 ± 5.1
De Boyer Montegut et al. (2004) h_m (T)	3.58 ± 0.14	118.5 ± 4.5	3.71 ± 0.14	126.4 ± 4.7
h_m of WOA94 (ρ)	66.92 ± 2.55	216.5 ± 8.3	157.34 ± 6.00	285.4 ± 10.3
	$6.78 \pm 0.23^*$	$207.2 \pm 7.1^*$	$7.67 \pm 0.26^*$	$215.1 \pm 7.6^*$
h_m of WOA94 (T)	377.28 ± 14.39	293.7 ± 11.2	374.72 ± 14.29	306.4 ± 11.6
	$7.12 \pm 0.24^*$	$208.5 \pm 7.2^*$	$8.00 \pm 0.27^*$	$218.0 \pm 7.4^*$
h_m from WOA01 (ρ)	3.86 ± 0.15	220.3 ± 8.4	5.18 ± 0.20	223.9 ± 8.5
h_m from WOA01 (T)	5.24 ± 0.20	186.8 ± 7.1	6.46 ± 0.25	191.8 ± 7.3
GRACE mean SSH	3.37 ± 0.12	131.1 ± 4.8	3.81 ± 0.14	141.1 ± 5.1
Rio05 mean SSH	3.36 ± 0.12	130.4 ± 4.8	3.80 ± 0.14	140.5 ± 5.1
$\kappa = 2000 \text{ m}^2 \text{ s}^{-1}$	3.27 ± 0.12	128.6 ± 4.9	3.69 ± 0.14	138.6 ± 5.2
NCEP–NCAR fluxes	3.76 ± 0.14	139.6 ± 5.2	4.53 ± 0.17	155.3 ± 5.6
	Flux climatologies defined as multiyear (10+) averages for each month			
SOC climatology	3.67 ± 0.13	142.0 ± 5.1	4.31 ± 0.15	157.4 ± 5.4
NCEP–NCAR climatology	3.35 ± 0.13	133.0 ± 5.0	3.82 ± 0.14	145.7 ± 5.3
NCEP II climatology	3.54 ± 0.14	133.6 ± 5.1	3.94 ± 0.15	144.3 ± 5.4
ECMWF climatology	3.47 ± 0.13	134.8 ± 5.1	3.91 ± 0.15	147.7 ± 5.4
COARE3.0 climatology	3.22 ± 0.12	126.8 ± 4.8	3.53 ± 0.13	135.2 ± 5.1

4. Sensitivity analysis

a. Sensitivity of the mixed layer heat balance to the choice of datasets

The heat budget results presented in section 3 are our best estimates from existing datasets (Table 1), with AMSR-E SST as T_m , h_m , and ΔT from Argo float profiles; sensible and latent heat fluxes from COARE3.0; longwave and shortwave radiative fluxes from the NCEP–NCAR reanalysis; geostrophic velocity from AVISO SSH anomalies; mean SSH from Maximenko and Niiler (2005); and Ekman velocity from COAPS winds. These data form our “base case” estimate of the upper-ocean heat budget. The base case has an rms(δ) of $3.26 \pm 0.12 \times 10^{-7} \text{ }^\circ\text{C s}^{-1}$ ($127.8 \pm 4.9 \text{ W m}^{-2}$), where the error bars are twice the standard error. To help evaluate how the uncertainties in these data influence the mixed layer heat budget, in this section we examine the sensitivity of the heat budget to the choice of datasets. A summary of the rms imbalances obtained in the sensitivity analysis is listed in Table 2. The left-most column indicates the variable that has been altered relative to the base case. Columns 2 and 3 show the rms(δ) in both degrees Celsius per second and watts per squared meter, corresponding to temperature tendency and heat flux, respectively. Units of watts per squared meter are converted from degrees Celsius per second by multiplying by $\rho c_p h_m$. Thus, the values in watts per

squared meter represent different volumes of water and are not directly comparable, whereas the values in degrees Celsius per second correspond to temperature change and can be compared directly. A temperature tendency of $10^{-7} \text{ }^\circ\text{C s}^{-1}$ converts to a heat flux of 40 W m^{-2} for a mixed layer of 100 m.

Of all the observations used in the mixed layer heat budget, the net air–sea heat flux Q_{net} has the largest uncertainties because of the sparseness of the in situ observations. The large uncertainties can be easily seen by comparing the different flux products. The Q_{net} from NCEP–Department of Energy (DOE) Reanalysis II (hereafter NCEP II; Kanamitsu et al. 2000) and ECMWF (Uppala et al. 2005) are not available for the full duration of our study period; however, comparisons of Q_{net} from NCEP–NCAR and NCEP II with ECMWF during 2000–02 indicate that the rms differences between these fluxes can exceed 100 W m^{-2} , suggesting that the uncertainties in Q_{net} can contribute more than 100 W m^{-2} to the imbalance locally. The turbulent fluxes from the COARE3.0 algorithm and from NCEP–NCAR also differ by 100 W m^{-2} or more, in particular in the Brazil–Falkland confluence and Agulhas Return Current regions, though the overall difference between the heat budgets is about 12 W m^{-2} (Table 2). The NCEP II fluxes result in about the same rms imbalance in the heat budget as in the NCEP–NCAR fluxes for their overlapping period (June 2002–

December 2004). Some flux products are only available as climatologies, representing multiyear averages for each month. The monthly flux climatology from the Southampton Oceanography Centre (SOC; Grist and Josey 2003) is considered to be one of the best flux climatologies based on global energy balance and comparisons with buoy measurements (Grist and Josey 2003; Toole et al. 2004). Comparison of the SOC climatology and the NCEP–NCAR climatology shows that they differ by 50 W m^{-2} or more, particularly along the ACC. When we applied the monthly climatological fluxes to the heat budget, by simply interpolating those fluxes to the corresponding week of the year over our study period, we found that the NCEP–NCAR climatology gives a better heat balance compared to the SOC climatology (see Table 2). Interestingly, compared with the weekly averaged fluxes from the NCEP–NCAR, the monthly climatologies from COARE3.0, NCEP–NCAR, NCEP II, SOC, and ECMWF all reduce the rms imbalance in the heat budget (Table 2). In addition, the flux climatology from COARE3.0 also gives a marginal improvement over the base case heat budget (Table 2). This suggests that the time evolution of the mixed layer temperature is not captured by the air–sea heat flux products.

In Eq. (1), the surface heating, Ekman advection, and entrainment terms are all related to h_m . Therefore, any errors in h_m will result in errors in all three terms. Both density and temperature criteria have been used in the literature to define h_m . In particular, the temperature criterion is used when no salinity observations are available. In regions where salinity has a negligible effect, temperature and density criteria can both give similar values of h_m . However, salinity can influence the stratification of the Southern Ocean, so temperature alone may not define h_m correctly. To examine how well the temperature criterion determines h_m , we calculated h_m from Argo float profiles based on a 0.2°C difference from surface temperature (de Boyer Montegut et al. 2004). We also calculated a corresponding monthly climatological ΔT . Then, we applied this h_m and ΔT to the heat budget. This gives an $\text{rms}(\delta)$ of $3.37 \pm 0.13 \times 10^{-7} \text{ }^\circ\text{C s}^{-1}$ ($129.3 \pm 4.9 \text{ W m}^{-2}$), which is within the error bar of the base case $\text{rms}(\delta)$ (Table 2).

We also examined the sensitivity of the heat budget to h_m by making use of three publicly available monthly h_m climatologies. The first is from de Boyer Montegut et al. (2004), who computed h_m using either density or temperature criteria. As noted, the density-based h_m has substantial gaps in the Southern Ocean, and therefore we use the de Boyer Montegut et al. (2004) temperature-based h_m fields, which define h_m based on an absolute temperature difference of 0.2°C . The second

h_m product is from *World Ocean Atlas 1994* (WOA94). Both the temperature criterion ($\Delta T = 0.5^\circ\text{C}$) and the density criterion ($\Delta\rho = 0.125 \text{ kg m}^{-3}$) are used to determine h_m from WOA94 (Monterey and Levitus 1997). This product has been used widely in the literature (e.g., Timlin et al. 2002; Alexander et al. 2006). The third h_m we computed from *World Ocean Atlas 2001* (WOA01; Conkright et al. 2002), using the same temperature and density criteria as in WOA94. These h_m climatologies are derived from data that cover different time periods, which may explain some of their differences. Argo profiles used to derive our base case h_m are from over the same time period as the AMSR-E SST measurements. The rms imbalance for each h_m product is listed in Table 2. Recall that the values in watts per squared meter are not directly comparable because they represent different volumes of water; with equal values in degrees Celsius per second, a deeper mixed layer would result in a larger value in watts per squared meter. The results using h_m from WOA94 give the largest imbalance with $\text{rms}(\delta)$ of $66.92 \pm 2.55 \times 10^{-7} \text{ }^\circ\text{C s}^{-1}$ ($216.5 \pm 8.3 \text{ W m}^{-2}$), whereas the heat budget based on h_m from de Boyer Montegut et al. (2004) gives results that are comparable to our best case. [Note that the small values in watts per squared meter for h_m of de Boyer Montegut et al. (2004) are due to their shallower mixed layer depth.] The large $\text{rms}(\delta)$ for WOA94 is mainly due to outliers in the western Indian Ocean, where in some places h_m is too shallow, and as a result the turbulent kinetic energy balance assumes a large entrainment velocity. After removing those outliers with $\delta > 5 \times 10^{-6} \text{ }^\circ\text{C s}^{-1}$, $\text{rms}(\delta)$ is significantly reduced but is still twice the $\text{rms}(\delta)$ of our base case (Table 2). The WOA94 and WOA01 both produce smaller $\text{rms}(\delta)$ values when h_m is computed using the density criterion (Table 2). Taken together, these results suggest that we need both temperature and salinity to define h_m in order to close the mixed layer heat budget in the Southern Ocean. Furthermore, the large difference in the imbalances obtained by using different h_m values suggests that studies of the upper-ocean heat budget depend on having correct values of h_m .

As discussed in section 2, salinity not only determines h_m , but it is also important for defining ΔT in the entrainment term of (1). To assess the importance of using time-varying climatological ΔT values, we recalculated the heat budget for all cases with a constant ΔT of 0.2°C , which corresponds to determining h_m from $\Delta\rho = 0.03 \text{ kg m}^{-3}$ if the salinity effect is ignored. The results are listed in the two columns on the right in Table 2. For all cases, the spatially varying ΔT gives better heat budget results with about a 10 W m^{-2} decrease in $\text{rms}(\delta)$, on average. Differences mainly occur during fall and

winter when the entrainment is strong. Using spatially varying ΔT , the domain-averaged imbalance is reduced by 38 W m^{-2} during winter. The largest improvement is in the Indian Ocean ($40^\circ\text{--}50^\circ\text{S}$, $70^\circ\text{--}150^\circ\text{E}$), where ΔT is mostly negative (Fig. 5).

Ekman heat advection may be sensitive to assumptions about the Ekman depth, which is the depth of penetration of the wind-driven flow (Chereskin and Roemmich 1991). In this study, we use h_m as the Ekman depth. In cases where the true Ekman depth is shallower than h_m , the Ekman advection is confined to the mixed layer, and the Ekman depth does not influence the heat budget. However, if the Ekman depth is deeper than h_m , the Ekman velocities will be overestimated, resulting in an overestimate of the cooling effect of Ekman advection in the mixed layer. Ekman transport has been observed to penetrate deeper than h_m at low latitudes in all three major oceans (Chereskin and Roemmich 1991; Chereskin and Price 2001). To test the sensitivity of the mixed layer heat budget to a deeper Ekman depth, we increased the Ekman depth by 50% of h_m , which effectively reduces Ekman transport within the mixed layer to two-thirds of its original value. The rms imbalance decreases by only 3 W m^{-2} , which suggests that the mixed layer heat budget in the Southern Ocean is not sensitive to the choice to use h_m as the Ekman depth.

Marshall et al. (2006) found that the diffusivity in the Southern Ocean varies between 500 and $2000 \text{ m}^2 \text{ s}^{-1}$. Increasing κ from 500 to $2000 \text{ m}^2 \text{ s}^{-1}$ changes the rms imbalance of the mixed layer heat budget by less than 1 W m^{-2} , suggesting that the heat budget results are not sensitive to the diffusivity.

Finally, we examined mean SSHs from GRACE (Tapley et al. 2003) and AVISO (Rio05; Rio and Hernandez 2004) as alternatives to the Maximenko and Niiler (2005) mean used in the base case. The rms imbalances from these three cases differed by less than 4 W m^{-2} , which is within the error bars of the base case (Table 2), suggesting that the heat budget is not sensitive to the choice of mean dynamic topography.

b. Sensitivity of water mass transformation to air–sea heat flux products

Air–sea heat fluxes act to convert surface water from one density class to another. Following Tziperman (1986), Speer and Tziperman (1992) suggested a formula for representing water mass transformation resulting from air–sea heat fluxes. Their method can be thought of as a recasting of the Q_{net} term on the right-hand side of (1) in order to represent water mass density conversion associated with the air–sea heat flux. Here this transformation is expressed in kilograms per

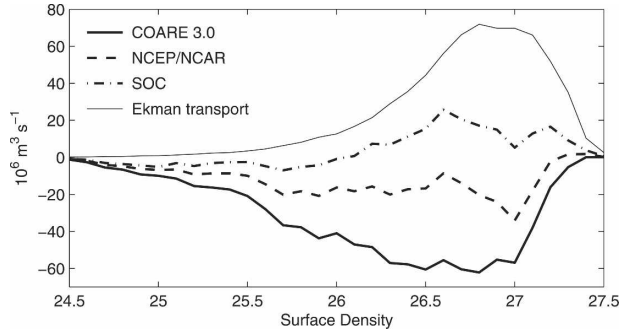


FIG. 12. Water mass transformation rates ($10^6 \text{ m}^3 \text{ s}^{-1}$) calculated using monthly climatological fluxes from COARE3.0 (thick solid line), NCEP–NCAR (dashed line), and SOC (dashed-dot line), and the northward Ekman transport (thin solid line). Negative values of the transformation rate mean warming and a transfer to lighter densities.

second per increment of density (or equivalently in cubic meters per second):

$$F(\rho) = \frac{1}{\Delta\rho} \sum \Delta A_{i,j} \left(\frac{-\alpha Q_{\text{net}}}{c_p} \right)_{i,j} \Pi(\rho - \rho'), \quad (3)$$

where $\Delta A_{i,j}$ is the area corresponding to the $1^\circ \times 1^\circ$ grid in our study region, which changes with latitude; $\Pi(\rho - \rho')$ is a rectangle function; and $\Delta\rho$ is the density bin width, chosen to be 0.1 kg m^{-3} in our calculations. The coefficient of thermal expansion of seawater (α) and the specific heat of seawater (c_p) are computed for each density bin using appropriate surface temperature and salinity derived from WOA01.

We calculated $F(\rho)$ using the monthly climatological fluxes from COARE3.0, NCEP–NCAR, and SOC, and then annually averaged (Fig. 12). As Karstensen and Quadfasel (2002) noted, the transformation rate can be quite sensitive to variations in heat fluxes. Figure 12 shows transformation rates differing by more than $70 \times 10^6 \text{ m}^3 \text{ s}^{-1}$, depending on the flux product used. For COARE3.0 fluxes, $F(\rho)$ reaches an extreme of $-60 \times 10^6 \text{ m}^3 \text{ s}^{-1}$ at 26.8 kg m^{-3} . If the mixed layer buoyancy budget is dominated by a balance between surface heat flux and northward Ekman transport, then $F(\rho)$ should balance the northward Ekman transport (thin line in Fig. 12), and this is roughly the case when COARE3.0 fluxes are used. In contrast, using a different surface flux product, Speer et al. (2000) found a less clear agreement between $F(\rho)$ and Ekman transport. Salinity effects and other terms in (1) may also account for any imbalance between $F(\rho)$ and the Ekman transport.

The derivative of $F(\rho)$ indicates the rate of water mass formation in one density class relative to the next (Speer and Tziperman 1992). All three flux climatologies agree in showing strong water mass formation processes in the density range between 27 and 27.2 kg m^{-3}

(as indicated by strong curvature in Fig. 12), corresponding to the region near the polar front and just to its south, as Speer et al. (2000) also noted. Thus, water mass formation appears to be strongest slightly south of mode water formation areas, which are associated with the sub-Antarctic front (Hanawa and Talley 2001). Overall, the $60 \times 10^6 \text{ m}^3 \text{ s}^{-1}$ maximum $F(\rho)$ and Ekman transport rates are more than double the values inferred by Speer et al. (2000) and roughly balance the total southward geostrophic transport of $50 \times 10^6 \text{ m}^3 \text{ s}^{-1}$ (Sloyan and Rintoul 2001).

5. Conclusions

In this study, the upper-ocean heat balance in the Southern Ocean has been examined by combining remotely sensed measurements and in situ observations. Here we use AMSR-E SSTs to represent the mixed layer temperature, sensible and latent heat fluxes from the COARE3.0 algorithm using NCEP–NCAR variables, longwave and shortwave radiative fluxes from the NCEP–NCAR, geostrophic velocities derived from AVISO SSH, Ekman velocities derived from COAPS wind, and finally the mixed layer depth and the temperature difference between the mixed layer and the base of the mixed layer from Argo float profiles. The mixed layer temperature undergoes a strong seasonal cycle that is most likely attributable to air–sea heat fluxes, because they are of about the same magnitude as the temperature tendency. Entrainment plays a secondary role. Oceanic advection also experiences a seasonal cycle, although it is relatively weak. The domain-averaged entrainment and advection are always negative throughout the year. In western boundary current regions, geostrophic advection plays an important role in upper-ocean heat budgets. However, in the Southern Ocean, geostrophic advection plays a minimal role because of the zonal alignment of the SSH and the SST contours. The meridional Ekman advection dominates total advection due to the large westerly winds in the Southern Ocean.

While the domain-averaged balance of heat advection, entrainment, diffusion, and air–sea heat fluxes is largely consistent with the evolution of the mixed layer heat content, substantial imbalances exist in the regional heat budgets. Large discrepancies between temperature tendency and the sum of contributions from surface heating, advection, diffusion, and entrainment are found in the Brazil–Falkland confluence and Agulhas Return Current regions. The largest imbalance in heat content is near the northern boundary of the ACC where the temperature gradient is large and air–sea coupling is expected to be strong (Hanawa and Talley 2001). The imbalance also shows a seasonal cycle

with larger imbalance during winter when O’Neill et al. (2005) noted that the winds responded strongly to the underlying SST. This suggests that the complex feedback processes of the coupling system in these regions are not well resolved by the existing measurements.

Differences between the various air–sea heat flux products for the Southern Ocean are large during winter. These discrepancies in the flux estimates most likely occur because of the sparseness of the in situ observations, and they imply uncertainties in the fluxes. The COARE 3.0 algorithm applied to variables from NCEP–NCAR improves the sensible and latent fluxes relative to the NCEP–NCAR fluxes. However, because of the large decorrelation scale of the NCEP–NCAR variables, both sets of fluxes appear to be too smooth, and do not resolve the small-scale features shown in the advection term. More interestingly, compared to the weekly averaged fluxes from COARE3.0 and NCEP–NCAR, the monthly climatological heat fluxes from COARE3.0, NCEP–NCAR, NCEP II, ECMWF, and SOC all give better heat budget results, suggesting that the time evolution of the mixed layer temperature is not well captured by the air–sea heat flux products. To close the local mixed layer heat budget in the Southern Ocean, a better air–sea heat flux product that resolves the small-scale structure and the time evolution of the mixed layer temperature is needed. Accurate surface heat flux estimates are also important for determining water mass transformation at the ocean surface, which is hypothesized to govern the global overturning circulation.

Our sensitivity tests suggest that a proper representation of the mixed layer depth is also important to close the heat budget. The seasonal cycle in the mixed layer depth is the main contributor to the seasonal variations in the advection term. Both temperature and density criteria have been used to define mixed layer depth. In regions where salinity has a negligible effect, temperature and density criteria both give similar values of mixed layer depth. However, salinity can influence the stratification of the Southern Ocean, so temperature alone cannot provide good mixed layer depth estimates. Our examination using the mixed layer depth based on density and temperature criteria suggests that the mixed layer depths determined using the density criterion result in a better heat balance. Salinity is also important for defining the temperature of the water entrained into the mixed layer from below. Because salinity changes can compensate for temperature, water below the mixed layer can be warmer than water within the mixed layer and entrainment can therefore warm the mixed layer. In view of the importance of salinity in the Southern Ocean, new measurements of salinity would be beneficial for understanding the

Southern Ocean climate system. Because we only resolve the seasonal variations in the mixed layer depth, which plays an important role in advection, the unresolved interannual variability of the mixed layer depth may also play a role in closing the mixed layer heat budget. The increasing number of Argo float profiles in the Southern Ocean may eventually provide a better estimate of the interannual variability of the mixed layer depth.

Overall, with the currently available data, our best estimate of the mixed layer heat budget in the Southern Ocean has a root-mean-squared imbalance of $127.8 \pm 4.9 \text{ W m}^{-2}$, which is dominated by winter imbalances in regions where the mixed layer is deep and the differences between air–sea heat flux products are large. This suggests that in situ observations (heat fluxes, temperature, and salinity profiles) in those regions would be particularly beneficial for evaluating air–sea heat fluxes and producing a better mixed layer depth estimate. Heat flux estimates with a spatial resolution of 0.25° would improve our understanding of the small-scale air–sea coupling processes. An improved heat flux field may be possible using satellite measurements of SSTs from AMSR-E, along with temperature and humidity profiles from the Atmosphere Infrared Sounder (AIRS), which is on the same satellite as AMSR-E. Ultimately, improved flux estimates and a more detailed understanding of upper-ocean processes in the Southern Ocean should improve our global view of how air–sea exchanges govern the meridional overturning circulation, mode water formation, and the global ocean heat budget.

Acknowledgments. The authors thank Dr. Teresa Chereskin and the two anonymous reviewers for helpful suggestions. This study is supported by NASA Grant EOS/03-0602-0117. The AMSR-E SSTs are produced by Remote Sensing Systems, available from <http://www.ssmi.com/>. The Argo float profiles are managed by the Global Ocean Data Assimilation Experiment, available from <http://www.usgodae.org/ftp/outgoing/argo/dac/>. The NCEP–NCAR and NCEP II variables are provided by the NOAA/OAR/ESRL PSD, in Boulder, Colorado, from their Web site at <http://www.cdc.noaa.gov/>. The altimeter SSH anomalies, produced by Ssalto/Duacs and distributed by Aviso with support from Centre National d'Etudes Spatiales, are available at <http://www.jason.oceanobs.com/html/donnees/produits/>. The 4-times daily fields of pseudo-stress are produced at COAPS and available from <http://www.coaps.fsu.edu/scatterometry/Qscat/>. The WOA94 mixed layer depths are available from the NOAA/Climate Diagnostics Center.

REFERENCES

- Alexander, M., and Coauthors, 2006: Extratropical atmosphere–ocean variability in CCSM3. *J. Climate*, **19**, 2496–2525.
- Barsugli, J. J., and D. S. Battisti, 1998: The basic effects of atmosphere–ocean thermal coupling on midlatitude variability. *J. Atmos. Sci.*, **55**, 477–493.
- Bladé, I., 1997: The influence of midlatitude ocean–atmosphere coupling on the low-frequency variability of a GCM. Part I: No tropical SST forcing. *J. Climate*, **10**, 2087–2106.
- Caldeira, K., and P. B. Duffy, 2000: The role of the Southern Ocean in uptake and storage of anthropogenic carbon dioxide. *Science*, **287**, 620–622.
- Chelton, D. B., M. G. Schlax, M. H. Freilich, and R. F. Milliff, 2004: Satellite measurements reveal persistent small-scale features in ocean winds. *Science*, **303**, 978–983.
- Chereskin, T. K., and D. Roemmich, 1991: A comparison of measured and wind-derived Ekman transport at 11°N in the Atlantic Ocean. *J. Phys. Oceanogr.*, **21**, 869–878.
- , and J. F. Price, 2001: Ekman transport and pumping. *Encyclopedia of Ocean Sciences*, J. H. Steele et al., Eds., Academic Press, 809–815.
- Conkright, M. E., and Coauthors, 2002: *Introduction*. Vol. 1. *World Ocean Atlas 2001*, NOAA Atlas NESDIS 42, 167 pp.
- de Boyer Montegut, C., G. Macde, A. S. Fischer, A. Lazar, and D. Iudicone, 2004: Mixed layer depth over the global ocean: An examination of profile data and a profile-based climatology. *J. Geophys. Res.*, **109**, C12003, doi:10.1029/2004JC002378.
- Dong, S., and K. A. Kelly, 2004: Heat budget in the Gulf Stream region: The importance of heat storage and advection. *J. Phys. Oceanogr.*, **34**, 1214–1231.
- , J. Sprintall, and S. T. Gille, 2006a: Location of the Antarctic polar front from AMSR-E satellite sea surface temperature measurements. *J. Phys. Oceanogr.*, **36**, 2075–2089.
- , S. T. Gille, J. Sprintall, and C. Gentemann, 2006b: Validation of the Advanced Microwave Scanning Radiometer for the Earth Observing System (AMSR-E) sea surface temperature in the Southern Ocean. *J. Geophys. Res.*, **111**, C04002, doi:10.1029/2005JC002934.
- Ducet, N., P.-Y. Le Traon, and G. Reverdin, 2000: Global high-resolution mapping of ocean circulation from Topex/Poseidon and ERS-1 and -2. *J. Geophys. Res.*, **105**, 19 477–19 498.
- Fairall, C. W., E. F. Bradley, J. E. Hare, A. A. Grachev, and J. B. Edson, 2003: Bulk parameterization of air–sea fluxes: Updates and verification for the COARE algorithm. *J. Climate*, **16**, 571–591.
- Gille, S. T., 2005: Statistical characterization of zonal and meridional ocean wind stress. *J. Atmos. Oceanic Technol.*, **22**, 1353–1372.
- Gould, J., and Coauthors, 2004: Argo profiling floats bring new era of in situ ocean observations. *Eos, Trans. Amer. Geophys. Union*, **85**, 185.
- Grist, J. P., and S. A. Josey, 2003: Inverse analysis adjustment of the SOC air–sea flux climatology using ocean heat transport constraints. *J. Climate*, **16**, 3274–3295.
- Hanawa, K., and L. D. Talley, 2001: Mode waters. *Ocean Circulation and Climate: Observing and Modelling the Global Ocean*, G. Siedler et al., Eds., International Geophysics Series, Vol. 77, Academic Press, 373–386.
- Jerlov, N. G., 1968: *Optical Oceanography*. Elsevier, 199 pp.
- Kalnay, E., and Coauthors, 1996: The NCEP/NCAR 40-Year Reanalysis Project. *Bull. Amer. Meteor. Soc.*, **77**, 437–471.

- Kanamitsu, M., W. Ebisuzaki, J. Woollen, J. Potter, and M. Fiorion, 2000: An overview of NCEP/DOE Reanalysis-2. *Proc. Second WCRP Int. Conf. on Reanalysis*, Reading, United Kingdom, WMO, 1–4.
- Karsten, R. H., and J. Marshall, 2002: Constructing the residual circulation of the ACC from observations. *J. Phys. Oceanogr.*, **32**, 3315–3327.
- Karstensen, J., and D. Quadfasel, 2002: Formation of Southern Hemisphere thermocline waters: Water mass conversion and subduction. *J. Phys. Oceanogr.*, **32**, 3020–3038.
- Marshall, J., and T. Radko, 2003: Residual-mean solutions for the Antarctic Circumpolar Current and its associated overturning circulation. *J. Phys. Oceanogr.*, **33**, 2341–2354.
- , E. Shuckburgh, H. Jones, and C. Hill, 2006: Estimates and implications of surface eddy diffusivity in the Southern Ocean derived from tracer transport. *J. Phys. Oceanogr.*, **36**, 1806–1821.
- Maximenko, N. A., and P. P. Niiler, 2005: Hybrid decade-mean global sea level with mesoscale resolution. *Recent Advances in Marine Science and Technology, 2004*, N. Saxena, Ed., PACON International, 55–59.
- Monterey, G. I., and S. Levitus, 1997: Climatological cycle of mixed layer depth in the World Ocean. U.S. Government Printing Office, National Oceanic and Atmospheric Administration, National Environmental Satellite, Data, and Information Service, 5 pp.
- Moore, J. K., and M. R. Abbott, 2000: Phytoplankton chlorophyll distributions and primary production in the Southern Ocean. *J. Geophys. Res.*, **105**, 28 709–28 722.
- Naveira Garabato, A. C., K. L. Polzin, B. A. King, K. J. Heywood, and M. Visbeck, 2004: Widespread intense turbulent mixing in the Southern Ocean. *Science*, **303**, 210–213.
- O'Neill, L. W., D. B. Chelton, and S. K. Esbensen, 2003: Observations of SST-induced perturbations of the wind stress field over the Southern Ocean on seasonal timescales. *J. Climate*, **16**, 2340–2354.
- , —, —, and F. J. Wentz, 2005: High-resolution satellite measurements of the atmospheric boundary layer response to SST variations along the Agulhas Return Current. *J. Climate*, **18**, 2706–2723.
- Paulson, C. A., and J. J. Simpson, 1977: Irradiance measurements in the upper ocean. *J. Phys. Oceanogr.*, **7**, 952–956.
- Pegion, P. J., M. A. Bourassa, D. M. Legler, and J. J. O'Brien, 2000: Objectively derived daily “winds” from satellite scatterometer data. *Mon. Wea. Rev.*, **128**, 3150–3168.
- Pollard, R. T., M. I. Lucas, and J. F. Read, 2002: Physical controls on biogeochemical zonation in the Southern Ocean. *Deep-Sea Res. II*, **49**, 3289–3305.
- Qiu, B., 2000: Interannual variability of the Kuroshio Extension system and its impact on the wintertime SST field. *J. Phys. Oceanogr.*, **30**, 1486–1502.
- , and K. A. Kelly, 1993: Upper-ocean heat balance in the Kuroshio Extension region. *J. Phys. Oceanogr.*, **23**, 2027–2041.
- Renfrew, I. A., G. W. K. Moore, P. S. Guest, and K. Bumke, 2002: A comparison of surface layer and surface turbulent flux observations over the Labrador Sea with ECMWF and NCEP reanalyses. *J. Phys. Oceanogr.*, **32**, 383–400.
- Rio, M.-H., and F. Hernandez, 2004: A mean dynamic topography computed over the World Ocean from altimetry, in situ measurements, and a geoid model. *J. Geophys. Res.*, **109**, C12032, doi:10.1029/2003JC002226.
- Roemmich, D., 1983: Optimal estimation of hydrographic station data and derived fields. *J. Phys. Oceanogr.*, **13**, 1544–1549.
- , J. Gilson, J. Willis, P. Sutton, and K. Ridgway, 2005: Closing the time-varying mass and heat budgets for large ocean areas: The Tasman Box. *J. Climate*, **18**, 2330–2343.
- Sabine, C. L., and Coauthors, 2004: The oceanic sink for anthropogenic CO₂. *Science*, **305**, 367–371.
- Sallee, J., N. Wienders, K. Speer, and R. Morrow, 2006: Formation of subantarctic mode water in the southeastern Indian Ocean. *Ocean Dyn.*, **56**, 525–542.
- Sloyan, B. M., 2005: Spatial variability of mixing in the Southern Ocean. *Geophys. Res. Lett.*, **32**, L18603, doi:10.1029/2005GL023568.
- , and S. R. Rintoul, 2001: Circulation, renewal, and modification of Antarctic mode and intermediate water. *J. Phys. Oceanogr.*, **31**, 1005–1030.
- Speer, K., and E. Tziperman, 1992: Rates of water mass formation in the North Atlantic Ocean. *J. Phys. Oceanogr.*, **22**, 93–104.
- , S. R. Rintoul, and B. Sloyan, 2000: The diabatic Deacon cell. *J. Phys. Oceanogr.*, **30**, 3212–3222.
- Sun, C., and D. R. Watts, 2002: Heat flux carried by the Antarctic Circumpolar Current mean flow. *J. Geophys. Res.*, **107**, 3119, doi:10.1029/2001JC001187.
- Tapley, B. D., D. P. Chambers, S. Bettadpur, and J. C. Ries, 2003: Large scale ocean circulation from the GRACE GGM01 Geoid. *Geophys. Res. Lett.*, **30**, 2163, doi:10.1029/2003GL018622.
- Thompson, A. F., S. T. Gille, J. A. MacKinnon, and J. Sprintall, 2007: Spatial and temporal patterns of small-scale mixing in Drake Passage. *J. Phys. Oceanogr.*, **37**, 572–592.
- Timlin, M. S., M. A. Alexander, and C. Deser, 2002: On the re-emergence of North Atlantic SST anomalies. *J. Climate*, **15**, 2707–2712.
- Toole, J. M., H.-M. Zhang, and M. J. Caruso, 2004: Time-dependent internal energy budgets of the tropical warm water pools. *J. Climate*, **17**, 1398–1410.
- Tziperman, E., 1986: On the role of interior mixing and air-sea fluxes in determining the stratification and circulation of the oceans. *J. Phys. Oceanogr.*, **16**, 680–693.
- Uppala, S. M., and Coauthors, 2005: The ERA-40 re-analysis. *Quart. J. Roy. Meteor. Soc.*, **131**, 2961–3012.
- Vivier, F., K. A. Kelly, and L. Thompson, 2002: Heat budget in the Kuroshio Extension region: 1993–99. *J. Phys. Oceanogr.*, **32**, 3436–3454.
- Yelland, M., and P. K. Taylor, 1996: Wind stress measurements from the open ocean. *J. Phys. Oceanogr.*, **26**, 541–558.